nature communications

Article

https://doi.org/10.1038/s41467-024-51632-y

Efficient roller-driven elastocaloric refrigerator

Received: 17 April 2024

Accepted: 11 August 2024

Published online: 22 August 2024

Check for updates

Sijia Yao[1,4], Pengfei Dang[2,4], Yiming Li[1], Yao Wang[1], Xi Zhang[1], Ye Liu[1], Suxin Qian[1,3] ✉, Dezhen Xue[2] ✉ & Ya-Ling He[1] ✉

Elastocaloric cooling has experienced fast development over the past decade owing to its potential to reshape the refrigeration industry. While the solid-state elastocaloric refrigerant is emission-free, the efficiency of the state-of-the-art elastocaloric cooling systems is not sufficient yet to reduce carbon emissions during operation. In this study, we double the coefficient of performance, the most commonly used efficiency metric, via the synergy of material-level advances in TiNiCu and the system-level roller-driven mechanism capable of recovering kinetic energy. On the materials level, a 125% improvement in coefficient of performance is illustrated in TiNiCu compared to NiTi, empowered by the B2-B19 martensitic transformation with improved lattice compatibility and the grain boundary strengthening from the nanocrystalline structure. On the system level, owing to the properly sized angular momentum in rotating parts, 78% work recovery efficiency is reported, transcending the theoretical limit previously unattainable without kinetic energy recovery. This confluence of materials and mechanical innovations propels elastocaloric cooling systems into a new realm of efficiency and paves the way for their practical application.

During the very recent UN Climate Change Conference (COP28) in Dubai, over 60 countries signed the Global Cooling Pledge, aiming to reduce 68% of emissions in the cooling sector by 2050[1]. Such a compelling need is due to >20% primary energy consumption from billions of cooling systems around the globe that are responsible for maintaining thermal comfort for humans and IT hardware[2]. With the projected growing trend[3], emissions due to cooling were predicted to quintuple by 2050[4]. Today, hydrofluorocarbon refrigerants, each kilogram as devastating as tons of carbon emissions, generate ~ 30% of emissions from cooling systems, and this percentage is still increasing thanks to the accelerating shift towards sustainable energy sources. Many low-emission gas-phase refrigerants have been studied, yet flammability, toxicity, or environmental hazards associated with fluoride, are still major concerns limiting the extensive applications of these alternative refrigerants.

This unclear future of gas-phase refrigerants provides an opportunity for the development of caloric cooling technologies whose refrigerants are non-volatile solids and thereby emission-free. In the so-called caloric materials, applying an external field, such as a magnetic field[5], electric field[6], or mechanical stress, induces solid-state phase transitions that are accompanied by temperature change, a.k.a. the caloric effect[7]. Different forms of stress result in subclassifications of mechanocaloric cooling[8–13]. Among them, elastocaloric (eC) is driven by uniaxial stress and has been studied in both Shape Memory Alloys (SMAs)[14–16] and polymers[17]. In a thermomechanically treated NiTi binary alloy, the temperature change during unloading can exceed 30 K[18], which is a magnitude higher than all magnetocaloric and many electrocaloric materials under practical field intensities. In addition, with both the SMA materials and mechanical actuators available from the market, an engineer can ~~easily~~ assemble a functioning eC cooling system, and thus eC cooling has undergone fast development in the

[1]School of Energy and Power Engineering, Xi'an Jiaotong University, Xi'an 710049, China. [2]State Key Laboratory for Mechanical Behavior of Materials, Xi'an Jiaotong University, Xi'an 710049, China. [3]MOE Key Laboratory of Cryogenic Technology and Equipment, Xi'an Jiaotong University, Xi'an 710049, China. [4]These authors contributed equally: Sijia Yao, Pengfei Dang. ✉e-mail: qiansuxin@xjtu.edu.cn; xuedezhen@xjtu.edu.cn; yalinghe@mail.xjtu.edu.cn

past decade surpassing other caloric counterparts, manifested by more than twenty published prototypes to date[19–44].

Among these eC cooling systems, only a few featured work recovery[20,29,30,32,39,42], i.e. harvesting part of the unloading energy from SMA to reduce the net input energy thus achieving higher efficiency[45]. The existing work recovery configurations can be divided into two categories, the antiphase pair of SMAs cyclically recovering only the potential energy[20,29,30,32,39], and the rotary design continuously recovering both kinetic energy and potential energy[42,46]. In the first category, the initial unloading force in the unloaded SMA overwhelms the required loading force in the antagonistic SMA, leading to an overall negative net force that corresponds to the irrecoverable part of unloading energy[47]. In the second category, despite the absence of irrecoverable work, continuously rotating SMA requires compensation for the inevitable and nontrivial friction. Whether or not such friction work is larger than the recovered kinetic energy is still unknown. Naturally, a novel design based on cyclic operation with minimized friction that also retains kinetic energy recovery resembles a new paradigm for unloading work recovery.

Materials performance dictates the performance ceiling of any eC cooling system[48]. Consequently, endeavors in materials design have been focused on optimizing strain reversibility, minimizing hysteresis, and reducing driving stress[49–51]. While experimental efforts have yielded promising results at the laboratory scale, particularly with materials like TiNiCu showcasing reduced stress hysteresis and improved fatigue characteristics[52,53], their application in eC cooling systems has been confined to small-scale formats such as free-standing films[54]. Challenges persist in scaling up production and ensuring processability, hindering widespread and scaled-up applications. Thus, balancing performance and scalability through composition design and thermomechanical treatment is essential to unlock the full potential of these materials for practical eC cooling applications.

In this work, we developed a roller-driven eC refrigerator that recovered kinetic energy, such that the achieved work recovery efficiency was beyond the theoretical work recovery efficiency without harvesting kinetic energy. Following the common fluid-free design using direct contact heat exchange, two antiphase SMA ribbons relayed heat pumping via an intermediate heat exchanger, resulting in a large temperature span outperforming the adiabatic temperature change of each respective SMA. The nexus of materials manufacturing advances in TiNiCu and the new work recovery scheme through the roller-driven mechanism provided a systematic approach to concurrently improve both materials and system efficiency.

Results

Principle of the roller-driven eC refrigerator

To inherit the competence of kinetic energy recovery in a rotary eC cooling device while adopting the cyclic operating scheme to minimize friction, we proposed the roller-driven mechanism, as shown in Fig. 1a. The two SMA ribbons were vertically mounted to the edge of a roller made of die steel on one side, and were fastened to sliding carriages that were aligned to the roller on the other side, such that the two ribbons were stretched only in the vertical direction. The roller was powered by a motor (Fig. S1a) via a gearbox (Fig. S1b) for amplification of the torque. The two antiphase SMA ribbons were cyclically stretched by the roller (Supplementary Movie 1), which periodically rotated between the two end positions in Fig. 1a (Supplementary Movie 2). When the roller swung to position 1 (Fig. 1b) and remained static for heat exchange, SMA#2 was fully loaded and attached to the heat sink (Fig. S1c), and SMA#1 was fully unloaded and attached to the heat source (Fig. S1d), where direct contact heat exchange was achieved. Rotating the roller back in the reverse direction required an acceleration process from static to the nominal rotating speed, which was driven by the difference in torque between SMA#2 being unloaded and SMA#1 being loaded. Therefore, part of the unloading work (Fig. 1c) was stored in the form of kinetic energy in the roller as well as other rotating parts including the gearbox and the rotor, which would otherwise consume more input power. As the rotating speed reached steady, the input power to the motor could be further reduced by leveraging the unloading torque from SMA#2. The capability to recover part of the unloading energy to accelerate the rotating parts is a unique characteristic of the proposed roller-driven mechanism, serving as the key to achieving high work recovery efficiency.

The antiphase pair of SMA ribbons (Fig. 1d) relayed heat pumping in a cascade arrangement (Fig. 1b). After SMA#2 rejected heat to ambient through the heat sink, it was unloaded and then absorbed heat by direct contact with the Intermediate Heat Exchanger (IHX, Fig. S1e). Meanwhile, SMA#1 was loaded and attached to the IHX, rejecting heat to SMA#2 across the IHX. Thus, unloading SMA#1 could reach a lower temperature than the minimum temperature of cyclically loading SMA#1 alone, thereby facilitating a larger temperature span. The relayed pumping of heat from SMA#1 (low-temperature stage) to SMA#2 (high-temperature stage) is the key to achieving large temperature spans of over 20 K, as illustrated by the infrared image in Fig. 1e and Supplementary Movie 3.

Performance of TiNiCu ribbon

The roller-driven mechanism facilitates high efficiency of the mechanical system, while substituting TiNiCu ternary alloy for the baseline commercial grade NiTi alloy was proven to be a crucial material-level advancement in improving efficiency. We used two ~220 mm long (heat exchange length 120 mm) and ~0.6 mm thick TiNiCu ribbons in our roller-driven eC refrigerator, which is, to the best of our knowledge, the first time application of SMA other than commercial-grade NiTi on a macro scale cooling device, i.e. 10^2mm length and 10^1 grams.

The kilogram-level raw TiNiCu sheets were prepared through a series of processes including induction melting, forging, hot rolling, high-temperature annealing, cold rolling, and low-temperature annealing (see Method Section for detailed procedures). Resulting in a finely tuned structure, the TiNiCu ribbon showcases a nanocrystalline composition with an average grain size of ~50 nm, as evidenced by the bright-field and dark-field transmission electron microscope images (Fig. 2a). Analysis through energy dispersive X-ray spectroscopy (Fig. S3) confirms a chemical composition closely aligned with the nominal composition of $Ti_{49.2}Ni_{44.8}Cu_6$ (at.%). The designed composition, featuring a deficiency in titanium, serves to suppress the monoclinic B19′ Martensitic Transformation (MT) and thereby induce a metastable orthogonal B19 MT at the relatively low Cu content[55], as revealed by the in-situ X-ray diffraction patterns in Fig. 2b. Compared to commercial-grade NiTi that undergoes a B2-B19′ MT (Fig. S4), the B2-B19 MT in TiNiCu empowers better lattice compatibility at phase boundary[56], resulting in good reversibility of MT with a smaller thermal (Fig. S5) and stress hysteresis (Fig. 2c). Furthermore, the abundant grain boundaries remarkably strengthen the transforming matrix of TiNiCu (Fig. S6) and suppress the dislocation-induced plasticity during stress-driven MT, thereby enhancing the transformation reversibility and elevating the utilization of latent heat.

To stabilize the superelastic behavior, the TiNiCu and NiTi ribbons were subjected to several tens of loading and unloading training cycles at the strain rate of $10^{-3}\,s^{-1}$ to remove the residual strain. Post-training, the TiNiCu ribbon exhibits reduced stress hysteresis compared to commercial-grade NiTi, as depicted in Fig. S7. Temperature variation in the trained TiNiCu ribbon at various strain rates was examined, illustrating saturation at higher strain rates (Fig. 2d and Fig. 2e). Consequently, under nearly adiabatic conditions with a strain rate of $0.04\,s^{-1}$, the adiabatic temperature changes (ΔT_{ad}) reached 14.2 °C during loading and 11.3 °C during unloading. Notably, the temperature distribution is quite uniform with no Lüders band (Fig. 2f), owing to the sluggish stress-induced MT induced by the

https://doi.org/10.1038/s41467-024-51632-y

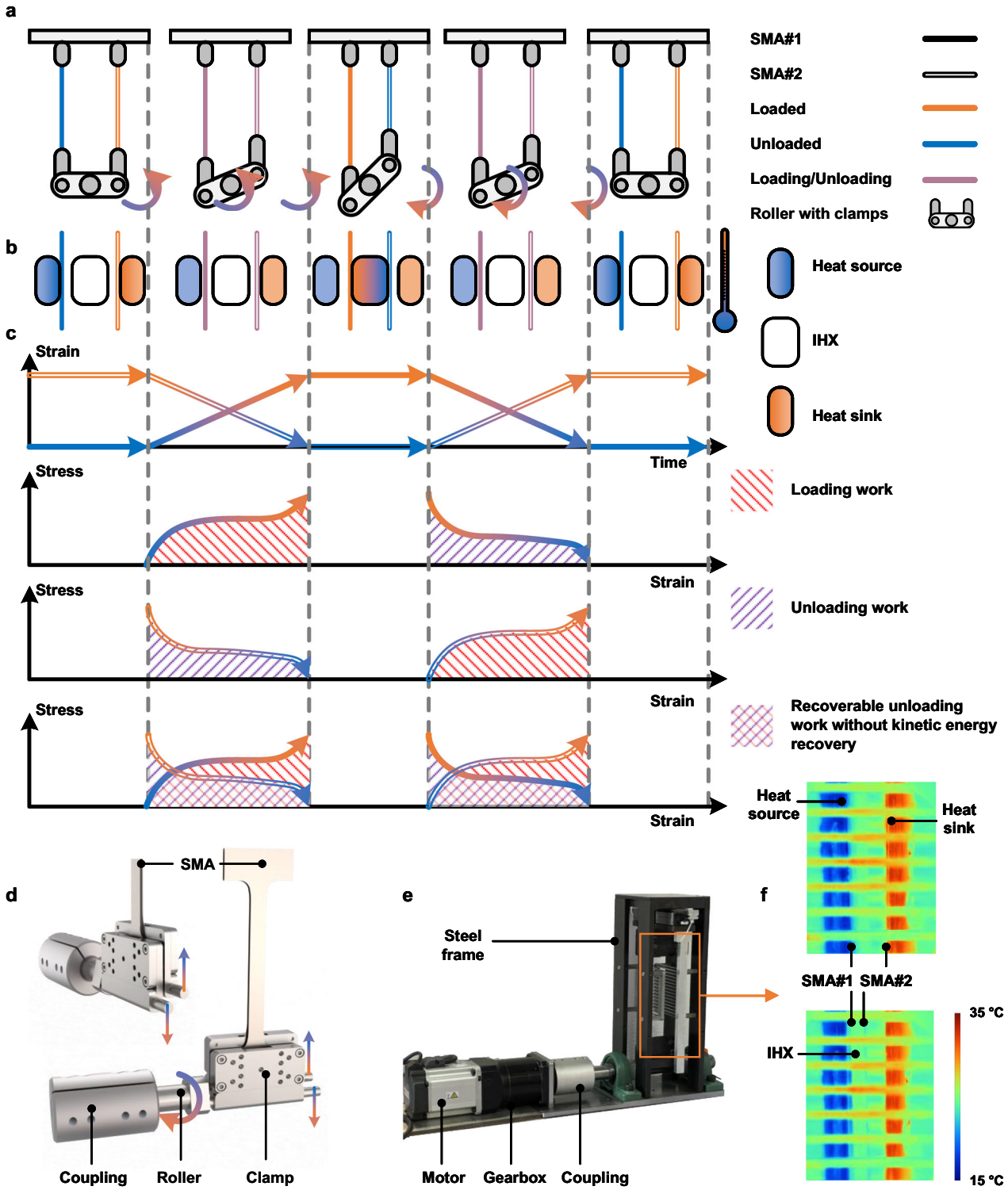

Fig. 1 | Principle of the roller-driven eC refrigerator. a driving mechanism. **b** illustration of cascaded eC cooling with two ribbons using direct contact heat exchange. **c** principle of work recovery. **d** 3-D model of the roller. **e** photo of the prototype. **f** infrared image of the heat sink, heat source, and intermediate heat exchanger (IHX) in the prototype. The horizontal bars are part of a frame that mounts the IHX, the heat sink, and the heat source.

nanocrystalline structure[57]. It facilitates efficient heat exchange with the heat source and heat sink. A comparison of ΔT_{ad} between the TiNiCu and commercial-grade NiTi ribbons across various strains was performed, and the results are illustrated in Fig. S8. While both exhibit a similar increasing trend of ΔT_{ad} within the low strain range, the unloading ΔT_{ad} of NiTi plateaus beyond 3.5% strain due to its inadequate strain recoverability. In contrast to the commercial-grade NiTi suffering from easy generation of dislocations, the addition of copper and the nanocrystalline structure in our TiNiCu alloy improve the lattice compatibility between the austenite and martensite phases and enhance the yield strength, thereby supporting a higher ΔT_{ad}. Figure 2g presents a comparative analysis of the eC performance between TiNiCu and commercial-grade NiTi ribbons under actual operation of the roller-driven eC refrigerator at around 4% strain after

https://doi.org/10.1038/s41467-024-51632-y

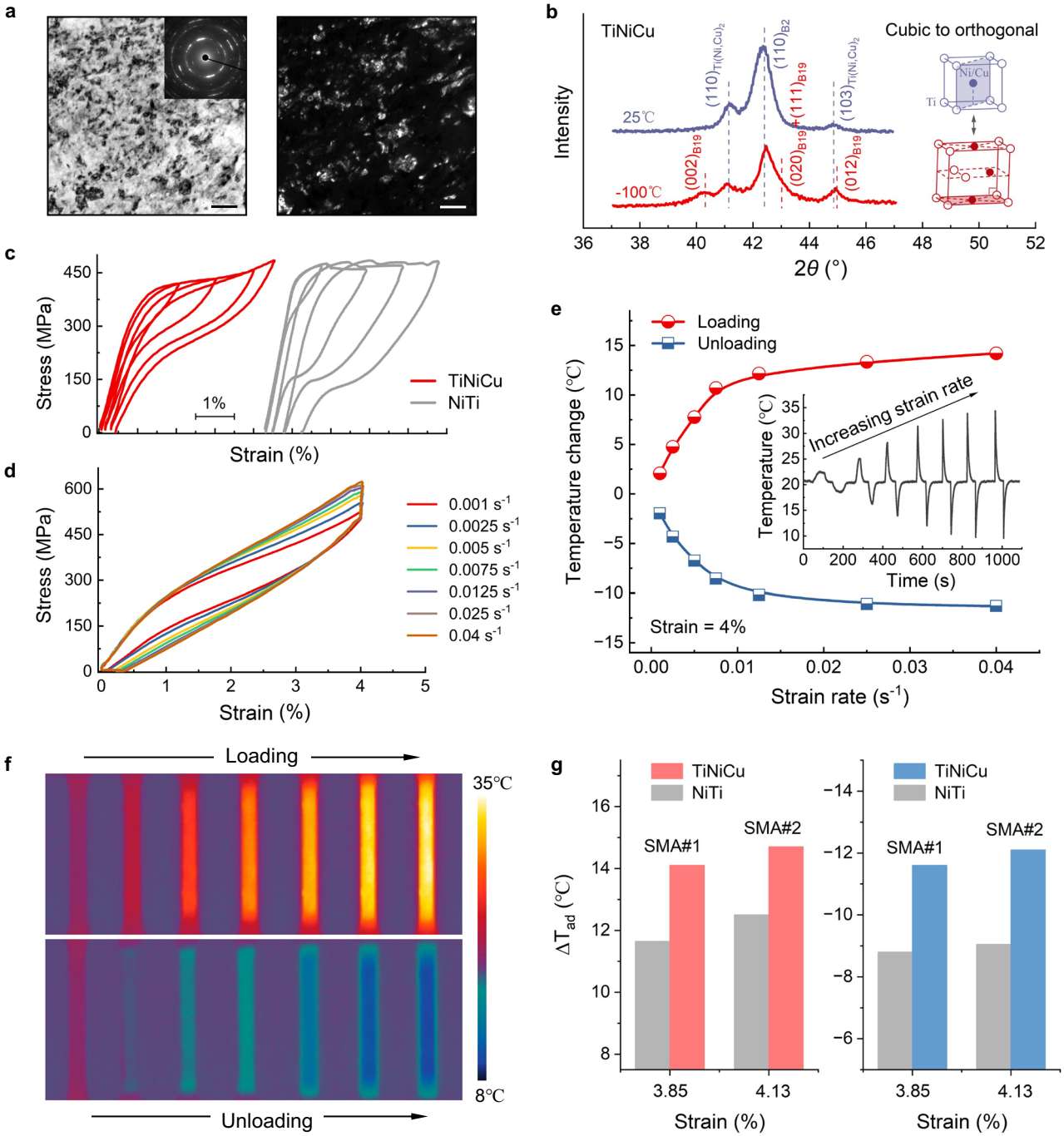

Fig. 2 | Microstructure and eC performance of TiNiCu ribbon used in the eC refrigerator. a bright-field and dark-field transmission electron microscope images showing a nanocrystalline structure in the TiNiCu ribbon. Scale bar, 200 nm. Inset is the corresponding electron diffraction pattern. **b** in-situ X-ray diffraction patterns showing a cubic to orthogonal MT during cooling. **c** isothermal stress-strain curves of TiNiCu ribbon show a smaller stress hysteresis compared to NiTi ribbon during the first four cycles. **d** stress-strain characteristics at different strain rates of trained TiNiCu ribbon. **e** temperature change at different strain rates of TiNiCu ribbon. Inset is the corresponding temperature-time curve. **f** infrared image of the TiNiCu ribbon during near adiabatic loading and unloading at the strain of 4%. **g** comparison of the adiabatic temperature change of TiNiCu and NiTi ribbons under operational strains during loading (left) and unloading (right). SMA#1 and SMA#2 refer to the two SMA ribbons specified in Fig. 1. The samples of both TiNiCu and NiTi alloys in (**d**–**g**) were taken from the ribbons used in the eC refrigerator and had undergone extensive pre-training.

extensive pre-training, revealing a remarkable enhancement in both ΔT_{ad} (25%) and material-level Coefficient of Performance, COP_{mat} (125%, see Methods for more details) for the TiNiCu ribbon.

Performance of the eC refrigerator

The two-stage cascade heat pumping realized a system temperature span transcending the adiabatic temperature change of the material, manifested by the large temperature span of 19.8 K using the commercial-grade NiTi (Fig. 3a) and 25.4 K with the new TiNiCu alloy (Fig. 3b). In both cases, the heat sink and heat source were insulated with zero heat load, and the temperature span reached steady after roughly 50 cycles (see Methods section for more details). Compared to their single-stage counterpart without relayed heat pumping (Fig. S9), the temperature span using NiTi and

https://doi.org/10.1038/s41467-024-51632-y

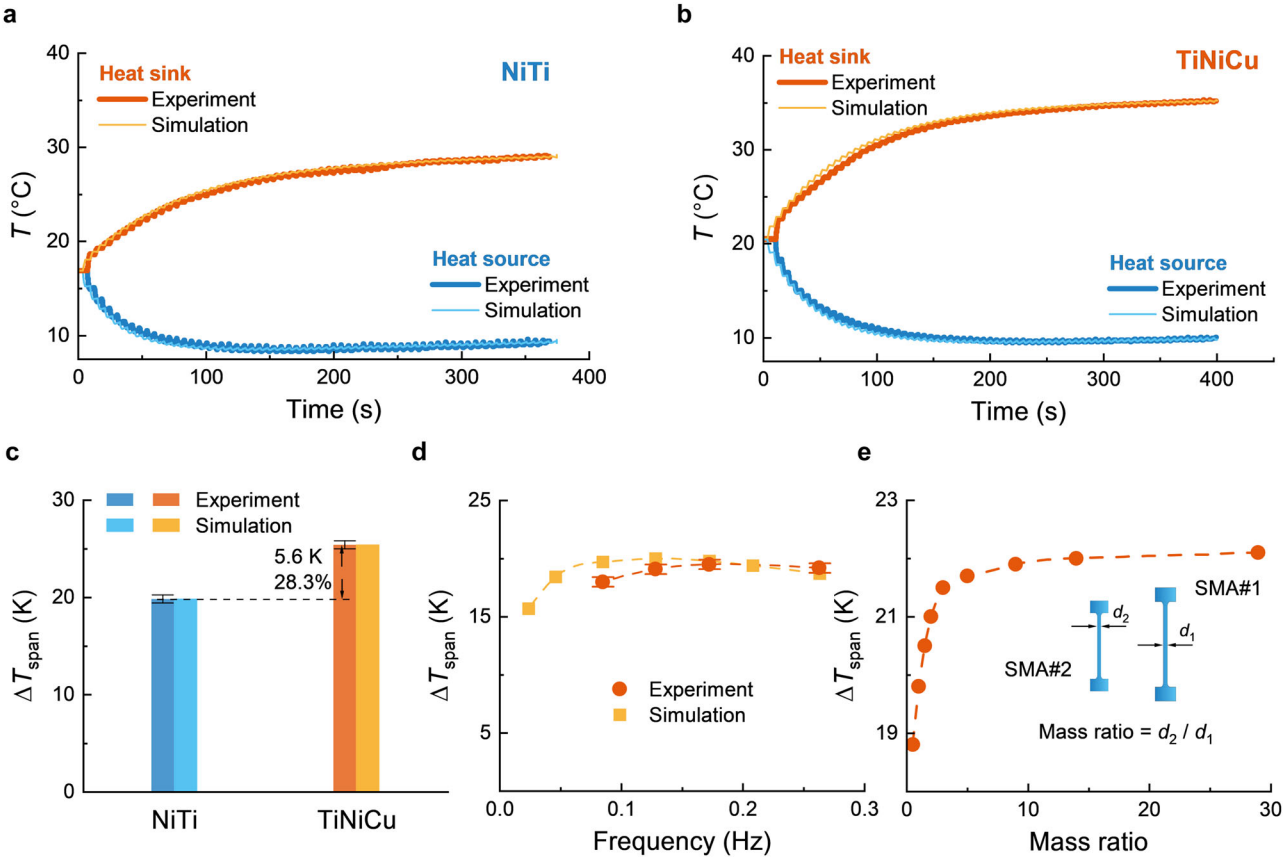

Fig. 3 | Load-free temperature span of the roller-driven eC refrigerator. **a** evolution of temperature span at 0.17 Hz using baseline commercial-grade NiTi ribbons (0.9 s for loading/unloading and 2 s for heat transfer). **b** evolution of temperature span at 0.17 Hz using TiNiCu ribbons. **c** Comparison of temperature span between NiTi and TiNiCu ribbons at 0.17 Hz. **d** frequency-dependent temperature span using baseline commercial-grade NiTi ribbons. **e** simulated temperature span with different NiTi mass ratios at 0.17 Hz. Mass ratio is the mass between SMA#2 (high-temperature stage) and SMA#1 (low-temperature stage). Error bars represent the measurement uncertainty of temperature span (see uncertainty analysis section in Supplementary Information).

TiNiCu was increased by 82% and 85%, respectively, at the same frequency of 0.17 Hz.

The 25% augmentation in the material-level adiabatic temperature change (Fig. 2g) in TiNiCu successfully converted to a 28% improvement in temperature span compared with the commercial-grade NiTi (Fig. 3c, and a consistent 26% improvement using a single SMA ribbon can be found in Fig. S9). This observation indicated that with proper system integration, the material-level enhancement can be proportionally translated into a boost in system cooling performance. Conversely, system cooling performance with new caloric materials can be reasonably projected by their caloric properties.

The above-mentioned temperature span was measured at an optimum frequency of 0.17 Hz (0.9 s loading, 2 s heat rejection, 0.9 s unloading, and 2 s cooling). This optimum frequency is slightly higher than the optimum frequency (0.15 Hz) in our previous NiTi wire-based refrigerator[34], because SMA ribbons had a larger contact area, a lower thermal contact resistance, and thereby superior heat transfer against the heat sink and the heat source than SMA wires (Fig. 3d and Fig. S10). Moreover, since the frequency-dependent temperature span is a result of the competition between heat loss and heat transfer effectiveness, a lower sensitivity of temperature span with regard to frequency (up to 1.5 K over frequency spectrum of 0.18 Hz) in this study indicated that the roller-driven eC refrigerator had better insulation and heat transfer (reduced thermal contact resistance) between the SMA and heat sink (source) than the wire-based refrigerator[34] (2.4 K over 0.22 Hz frequency spectrum). Reducing the thermal contact resistance by applying normal pressure and increasing contact area can further increase the optimum frequency and the optimum temperature span (Fig. S11).

The second SMA ribbon not only increases the temperature span but also introduces an additional degree of freedom in system design, which is the mass ratio between the two SMA ribbons. With the constraint of the total mass of 11.9 grams and constant materials thickness and length, varying the mass ratio between SMA#2—the high-temperature stage, and SMA#1—the low-temperature stage, leads to optimization of the cooling performance at a fixed cost, because the weight and cost of SMAs all remain unchanged. Using the experimentally validated dynamic system model (see Supplementary Information for model details), we predicted the temperature span with different mass ratios, ranging from 0.5 to 30 (Fig. 3e). A 22.1 K temperature span was predicted when the mass ratio was 30, representing 11.6% improvement from the baseline 1:1 design. The temperature span is not significantly affected by the mass ratio because, ideally, it should be an intensity variable independent of mass. However, mass ratios deviating from 1:1 impel the imbalance of (un)loading torque between SMA#1 and SMA#2, which may potentially degrade the work recovery performance. Consequently, it is not necessary to switch to asymmetric designs to pursue high temperature spans.

Since our goal is to deliver cooling below ambient temperature, the pull-down performance and cooling power were also important. At room temperature of 21 °C, the heat source temperature reached 10 °C after 154 s when using TiNiCu ribbons, which is 49% faster than the baseline NiTi ribbons (Fig. 4a). After 561 s, the heat source reached the minimum of 7.7 °C, which was 17.8 °C below the heat sink temperature and was also below the storage temperature requirement of wine

https://doi.org/10.1038/s41467-024-51632-y

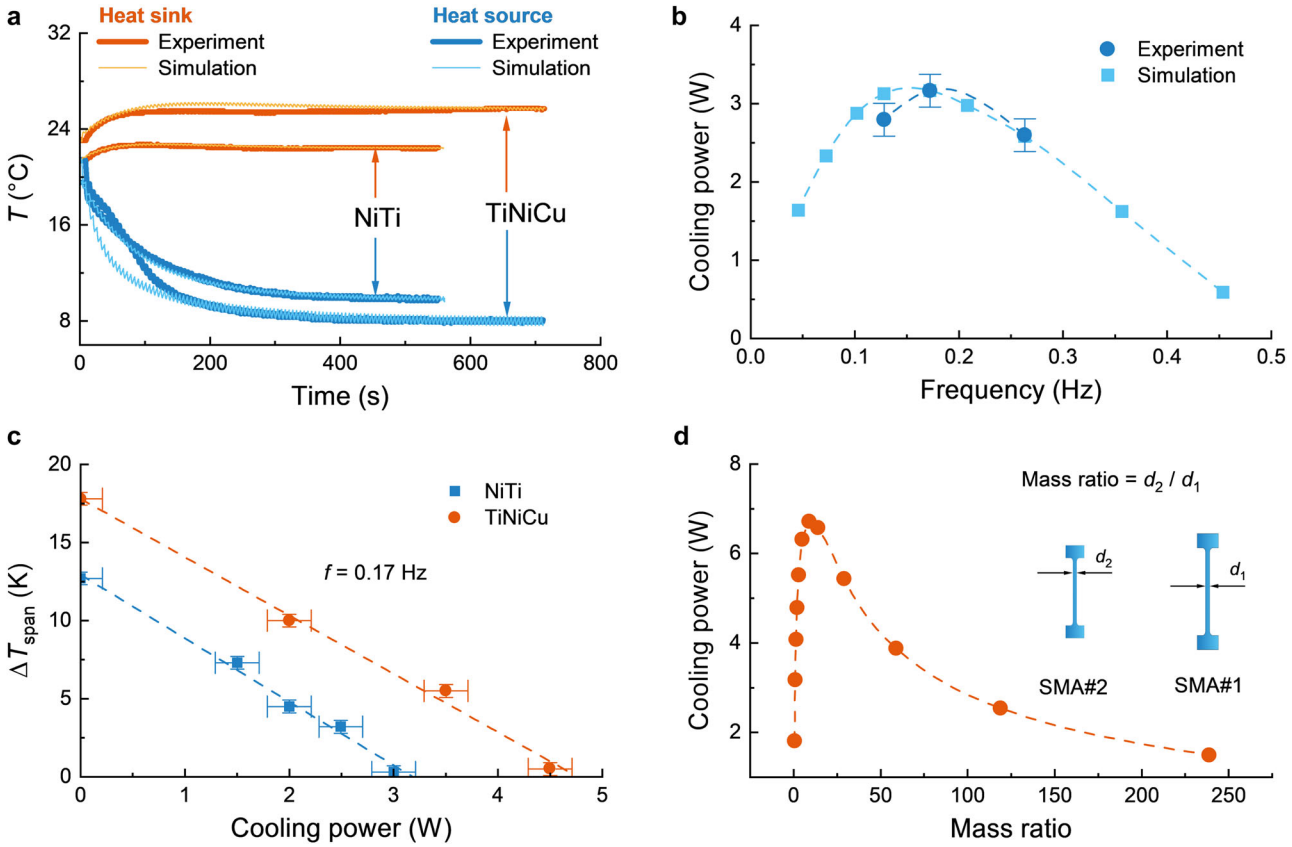

Fig. 4 | Cooling power of the roller-driven eC refrigerator. a pull-down temperature profile of NiTi and TiNiCu ribbons at 0.17 Hz when the heat sink is actively cooled by ambient air. **b** frequency-dependent cooling powers at zero temperature span using baseline NiTi ribbons. **c** Comparison of NiTi and TiNiCu on the cooling performance map at 0.17 Hz. **d** simulated cooling power with different NiTi mass ratios at 0.17 Hz and zero temperature span. Mass ratio is the mass between SMA#2 (high-temperature stage) and SMA#1 (low-temperature stage). Error bars represent the measurement uncertainty of temperature span or cooling power (see uncertainty analysis section in Supplementary Information).

refrigerators (12.8 °C). Although this target temperature could be achieved using a single TiNiCu ribbon (Fig. S12), at an elevated ambient temperature of 25 °C, the temperature span (10.9 °C) is no longer sufficient without cascading two SMAs.

We confirmed the optimum frequency of 0.17 Hz also applied to cooling power at zero temperature span (Fig. 4b). At the optimum frequency, the eC refrigerator with two TiNiCu ribbons achieved 4.5 W cooling power, resembling a 50% improvement from the baseline NiTi ribbons (3 W, Fig. 4c). The refrigeration temperature span of using two TiNiCu ribbons was 7.6 °C less than the load-free temperature span since the heat sink rejected part of the eC heat to the ambient. In this case, TiNiCu demonstrated 40% improvement (5.1 °C) against the commercial-grade NiTi, which was another indication for the reduced hysteresis in TiNiCu. Although relaying two SMA ribbons promoted the temperature span, there is always an additional temperature difference between the two SMA ribbons as the driving potential for heat exchange, which implies that part of the eC effect is neutralized inside the system. Following the tradition in vapor compression refrigeration, such a temperature difference was denoted as cascade temperature difference, which increased with cooling power (Fig. S13). As a result, the maximum cooling power using two cascaded SMA ribbons (Fig. 4c) was less than doubling the maximum cooling power of a single SMA ribbon (Fig. S12).

One way to mitigate the cascade temperature difference problem is by optimizing the mass ratio (Fig. 4d). First, because of hysteresis, in each SMA ribbon, the rejected heat is always more than the absorbed heat. Therefore, with the baseline 1:1 mass ratio, SMA#2 experiences a higher heat flux than SMA#1. With more mass on SMA#2, the heat flux from the IHX to SMA#2 can be reduced, thus reducing the cascade temperature difference. As a result, adding more materials to SMA#2 is effective in increasing cooling power. However, if the mass of SMA#1 falls below a threshold, there are no sufficient caloric materials to pump heat from the low-temperature heat source. Considering these two competing factors, the optimum mass ratio is 9, corresponding to a cooling power of 6.7 W, exceeding the 3.1 W cooling power with the symmetric mass ratio.

Efficient work recovery

The roller-driven eC refrigerator featured high-efficiency work recovery between the two antiphase SMA ribbons. With the recovered unloading work, the cycle-averaged input power to the actuator was reduced by 44% compared to the input power of loading two TiNiCu ribbons separately (Fig. 5a). In other words, loading the second TiNiCu ribbon was almost free. Since TiNiCu alloy was known for lower hysteresis, recovering its unloading energy was more cost-effective compared to the baseline NiTi[58], and therefore, the reduction of input power in the case of NiTi was less (36%).

To quantitatively evaluate the performance of work recovery, the theoretical work recovery efficiency without considering kinetic energy recovery was computed first, following the definition by Kabirifar et al. [47] (see Methods section and Supplementary Information for more details). This theoretical work recovery efficiency only depends on the stress-strain curve of the SMA, which is affected by materials properties, including hysteresis, elastic modulus, transformation strain, Clausius-Clapeyron coefficient, etc, and operating conditions, such as (un)loading rate and temperatures. The stress-strain curve at the same ambient temperature and (un)loading rate (Fig. 2a) was used to evaluate the theoretical work recovery efficiency. Based on

https://doi.org/10.1038/s41467-024-51632-y

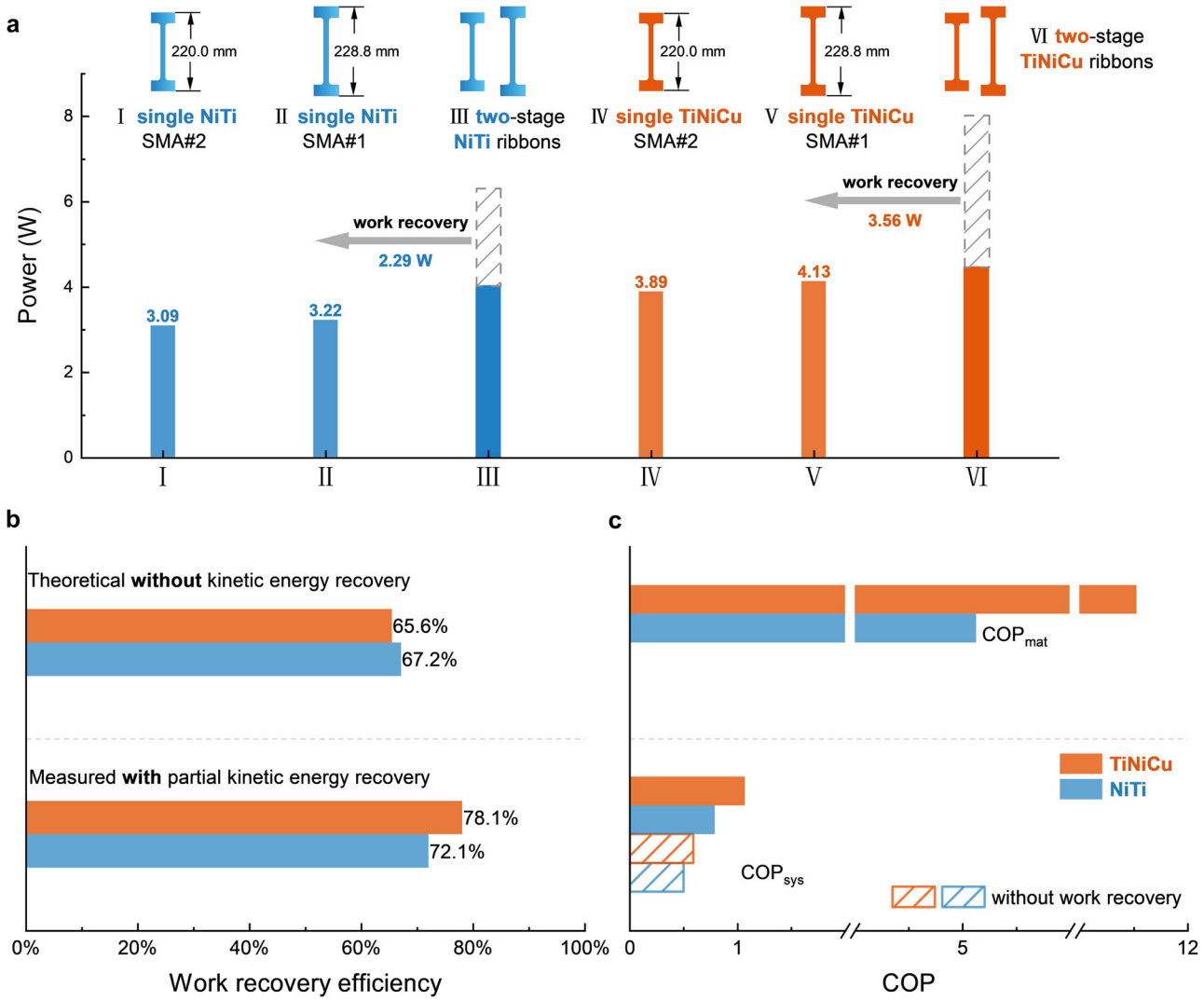

Fig. 5 | Coefficient of performance of the roller-driven eC refrigerator. **a** comparison of the time-averaged input power between a single SMA ribbon and two SMA ribbons at zero temperature span. **b** comparison of theoretical work recovery efficiency and measured work recovery efficiency. **c** coefficient of performance comparison between the baseline (without work recovery), system *COP* with work recovery, and materials *COP*, at zero temperature span, i.e. heat sink and heat source at ~ 294 K. The cooling power corresponding to the TiNiCu was 4.2 W at 0.12 Hz. The cooling power corresponding to the NiTi was 2.8 W at 0.12 Hz.

these, the two materials showed almost identical theoretical work recovery efficiency (Fig. 5b).

The novel roller-driven mechanism facilitates measured work recovery efficiencies surpassing their theoretical counterparts without kinetic energy recovery. The additional 12.6% work recovery efficiency in the case of TiNiCu was an indicator of a successful recovery of kinetic energy: the released unloading work from one SMA ribbon accelerated the rotating parts in the eC refrigerator, whereas such kinetic energy cannot be easily recovered in eC cooling systems with reciprocating antiphase SMAs. As far as we know, this is the first time measurement of work recovery efficiency, and also the first time report of recovering kinetic energy.

The high-efficiency work recovery leads to the measured system coefficient of performance (COP_{sys}, "plugged into electricity outlet" *COP*) of 1.27 superior to the baseline COP_{sys} of 0.70 without work recovery (Fig. 5c, see Methods section), both at zero temperature span (heat sink and heat source at ~ 294 K). The COP_{sys} of TiNiCu is 35% higher than NiTi, because of less hysteresis on the materials level, more caloric effect, and higher work recovery efficiency. Unfortunately, the system-level *COP* is still much less than the materials *COP*, i.e. 11.5 in TiNiCu and 5.1 in NiTi (see Methods section). More efficient utilization of the eC effect by promoting the heat transfer between SMA and solid-state heat exchangers has the potential to further increase the COP_{sys} to 2.5 (Fig. S14).

Discussion

We estimated the recovered kinetic energy based on the angular momentum of the rotating parts in the eC refrigerator (see Supplementary Information for more details). In each cycle, the acceleration of the rotating parts requires 0.72 J kinetic energy, whereas the difference in unloading work between the measured case with partial kinetic energy recovery and the theoretical limit without considering kinetic energy was 0.8 J (Fig. 5b). Considering the measurement and estimation uncertainties, this can be considered as a close match, which further supported the capability of recovering part of the kinetic energy in the proposed roller-driven mechanism. The acceleration or increase of angular momentum of the rotating assembly driven by the unloading energy can be visualized by the sharp variation of directly measured net torque (Fig. S17). From the same analysis, it is clear that further increasing the angular momentum of the rotating parts can theoretically recover even more kinetic energy and achieve a higher work recovery efficiency. However, an engineer should keep in mind the tradeoff between the margin of further increasing the work

recovery efficiency and the enlarged system weight and initial cost due to the rise in angular momentum. To achieve higher work recovery efficiency, continuous rotating is necessary. A specific design of the moving path of SMAs with sufficient quasi-stable time for direct contact heat exchange while maintaining a constant rotation speed of the actuator should be investigated in the future.

It is interesting to find out that an asymmetric mass ratio is beneficial to cooling power. In fact, this is consistent with the conventional wisdom in the refrigeration industry: a multi-stage cascade thermoelectric cooling module contains more materials in the high-temperature stage[59], such that the rejected heat from the low-temperature stage can be effectively handled by the proper amount of materials in the high-temperature stage. Similarly, a two-stage cascaded vapor compression refrigeration system features a higher flow rate and capacity also in the high-temperature stage[60]. However, the asymmetric mass ratio brings a new challenge of asymmetric unloading torque. How to maintain high unloading efficiency while optimizing cooling power via asymmetric mass ratio should be investigated in the future.

In a previously reported prototype[38], all SMAs were synchronized without any phase delay, whereas the two SMAs experienced a 180° phase difference from each other in this study (Fig. S15). The phase difference led to a slight variation in the heat transfer characteristics of the IHX. In the case of ref. 38, the IHX absorbed heat from SMA#1 in the first half cycle and then rejected heat to SMA#2 in the second half cycle, while in this study, SMA#1 simultaneously rejected heat to SMA2 through the IHX. Although the 180° phase difference is essential in the eC refrigerator to facilitate work recovery, our simulation results indicated that the phase difference had a trivial impact on both temperature span and cooling power (Table S2).

In summary, we developed an efficient fluid-free eC refrigerator by the synergy of macro-scale polycrystal TiNiCu alloy with higher intrinsic efficiency and kinetic energy recovery using a novel roller-driven mechanism. The nanocrystalline structure, coupled with the B2-B19 transformation pathway, confers upon the TiNiCu ribbon reduced hysteresis and enhanced utilization of latent heat. The relayed heat pumping successfully exceeded the materials' adiabatic temperature change by 1.1 times, thus achieving a load-free temperature span of 25.4 K and reaching a refrigeration temperature of 7.7 °C in 560 s at 0.17 Hz operating frequency. The 25% enhanced caloric effect in TiNiCu directly translated to a 28% improvement in temperature span from the baseline commercial-grade NiTi. The antiphase configuration with sufficient angular momentum in rotating parts effectively recovered 0.72 J kinetic energy per cycle, resulting in 78% work recovery efficiency that transcended the theoretical prediction of 65% without kinetic energy recovery. The nexus of efficient TiNiCu materials and high-efficiency work recovery resulted in a system *COP* of 1.27. More efficient utilization of the caloric effect by promoting the heat transfer between SMA and solid-state heat exchangers will hopefully thrust the system *COP* one more step closer to the materials *COP* of over 11.

Methods

Materials preparation

The commercial-grade NiTi ribbons with a nominal composition of $Ni_{50.8}Ti_{49.2}$ in atomic fraction were obtained from Baoji Seabird Metal Materials Co. Ltd. As received NiTi sheets were cut into target ribbon shapes. To achieve the kilogram-level TiNiCu sheet for producing multiple ribbons, a 7 kg alloy ingot with a nominal composition of $Ti_{49.2}Ni_{44.8}Cu_6$ (at.%) was prepared by induction melting. The ingot was forged and hot-rolled to obtain a sheet with a thickness of 0.85 mm. Then, the hot-rolled sheet was annealed at 900 °C for 0.6 ks to promote the dissolution of the second phase. The 0.85 mm sheet was then cold rolled at room temperature to further reduce its thickness to 0.64 mm, producing a thickness reduction of 25%. The cold-rolled ribbon was low-temperature annealed at 350 °C for 1.2 ks in order to obtain a nanocrystalline structure.

Materials characterization

The microstructure and chemical composition of the TiNiCu ribbon were analyzed using a JEM-F200 Transmission Electron Microscope (TEM) at room temperature equipped with an Energy Dispersive X-ray Spectrometer (EDS). Differential scanning calorimetry (DSC) measurements were performed using the Netzsch 214 calorimeter with a heating/cooling rate of 10 °C min^{-1}. The structural transformation upon cooling was determined by a Bruker D8 ADV ANCE X-Ray Diffractometer (XRD) with Cu Kα radiation. Tensile tests were conducted on the dog-bone samples by an Instron-5969 mechanical testing machine equipped with a video extensometer. The strain rate of 0.0005 and 0.04 s^{-1} was used to approximate the isothermal and adiabatic conditions, respectively. The temperature change was recorded by a K-type thermocouple welded on the surface of the samples. The temperature distribution on the surface of TiNiCu ribbon during quasi-adiabatic loading and unloading was captured by an infrared camera (FLIR A651).

Prototype characterization

Temperatures of the heat sink (hot side aluminum radiator), heat source (copper block), and intermediate heat exchanger (copper block) were measured using miniature T-type thermocouples with a type B standard uncertainty u_B of ±0.29 K (see Supplementary Information for more details). The temperature span of the eC refrigerator was determined by $\Delta T_{span} = \int_{t_1}^{t_2} (T_{sink} - T_{source})\,dt$ over the steady-state period.

The energy balance method was applied to directly measure cooling power. When the temperature span reaches the steady state, the input power to the heater equals the cooling power, i.e. $Q_c = P_{heater}$. A 0.2 mm thick polymer film heater was cut to fit the geometry of the copper block heat source. The polymer film heater was powered by a programmable DC power source (ITECH IT6942B) with a total uncertainty of ±0.2 W. To minimize heat loss to the ambient, 3 mm thick foam insulations were used to mount the polymer film heater.

The input power to the motor was measured by a power meter (Qingzhi 8775B1) with a total uncertainty of ±0.03 W.

The torque to the roller was measured by a torque meter (DAY-SENSOR DSN-200) that was installed between the roller and the output shaft of the gearbox (Fig. S2). The range of measured torque is from −200 Nm to 200 Nm, with an uncertainty of 0.2 Nm.

All analog signals were sampled at 20 Hz and recorded using NI cDAQ chassis, in which NI cDAQ 9214 module with cold-junction compensation was used to record temperature readings. The digital reading from the power meter and the torque meter was transmitted to LabVIEW following the RS485 protocol.

Work recovery efficiency

The work recovery efficiency evaluates the effectiveness of recovering unloading work and is defined as the ratio between recovered unloading work and total unloading work, as shown in Eq. (1).

$$\eta_{WR} = \frac{\text{recovered unloading work}}{\text{unloading work}} = 1 - \frac{\text{irrecoverable unloading work}}{\text{unloading work}} \tag{1}$$

In a typical antagonistic work recovery scheme, at the beginning of the unloading process, the unloaded eC unit releases the highest force, while the antiphase eC unit being loaded only requires the minimum force, resulting in a negative input force (Fig. S16). Without kinetic energy recovery, the unloading work in the negative input force region cannot be recovered[47], and this irrecoverable unloading work degrades the work recovery efficiency in Eq. (1).

In the case of the two-stage eC refrigerator, the mass and length of the two SMA ribbons are different. Thus, the loading/unloading stress-strain characteristics between the first half cycle and second half cycle are not identical, leading to a minor difference in irrecoverable

unloading work (Fig. S16). The irrecoverable unloading work is visually represented by the sum of two gray areas in Fig. S16, while the total unloading work is the sum of gray and blue areas. Due to the slight difference in mass, the first half and second half cycles should be integrated separately, i.e. irrecoverable unloading work $\cong |S_1| + |S_3|$, and unloading work $\cong |S_1 + S_2| + |S_3 + S_4|$, and details of the calculation can be found in Eqs. (S1-S3). Parameters are listed in Table S5.

The angular momentum in the roller can recover part of the unloading work in the negative input force region. The system work recovery was calculated using Eq. (2) based on measured data.

$$\eta_{WR,\,exp} = \frac{\left(\int_{SMA\#1} P\mathrm{d}t + \int_{SMA\#2} P\mathrm{d}t - \int_{SMA\#1+SMA\#2} P\mathrm{d}t\right)\eta_{mech}}{\left(|S_1 + S_2| + |S_3 + S_4|\right)V} \quad (2)$$

where P is the measured power, (W), and η_{mech} is the mechanical efficiency of the actuator. $|S_1 + S_2| + |S_3 + S_4|$ is a graphical representative of the unloading work, (J m^{-3}), and V is the volume of SMA, (m^3). Details of obtaining Eq. (2) can be found in Eqs. (S4-S10).

Coefficient of performance

The material-level *COP*, COP_{mat}, was calculated based on the commonly used definition at zero temperature span[13], i.e. $COP_{mat} = T_c(\Delta s - s_{gen})/[(T_h - T_c)\Delta s + (T_h + T_c)2s_{gen}]$, where Δs is entropy change due to martensitic transformation, (J kg^{-1} K^{-1}), determined by $\Delta s = \frac{c_p \Delta T_{ad}}{T_c}$. c_p is the specific heat capacity, (J kg^{-1} K^{-1}), ΔT_{ad} is the adiabatic temperature change during unloading, (K), T_h is the temperature of the heat sink (K), and T_c is the temperature of the heat source, (K). The entropy generation $s_{gen} = \oint \sigma \mathrm{d}\varepsilon / 2\rho T_0$, where $\oint \sigma \mathrm{d}\varepsilon$ denotes the enclosed area of the isothermal stress-strain curve at temperature of $T_0 = 22$ °C (Fig. S7).

The system-level *COP*, COP_{sys}, was calculated using the measured cooling power and the measured input power as $COP_{sys} = Q_c/W$, where Q_c denotes the measured cooling power at zero temperature span (W) and W is the time-averaged input power to the actuator (W). The input power to the actuator is the time average of instantaneous power over the loading time of both SMA ribbons, $W = \int_{SMA\#1+SMA\#2} P\mathrm{d}t / t_{loading,SMA\#1+SMA\#2}$.

The system-level *COP* without work recovery was estimated using the sum of time-averaged input power to the actuator when loading each SMA ribbon separately.

Parameters related to *COP* can be found in Table S6.

Data availability

The data supporting the findings of this study are included within the article and its Supplementary Information.

References

1. UNEP. *Global Cooling Watch 2023: Keeping it Chill*. https://wedocs.unep.org/handle/20.500.11822/44243 (2023).
2. Dupont, J. L., Domanski, P. A., Lebrun, P. & Ziegler, F. *The Role of Refrigeration in the Global Economy*. https://iifir.org/en/fridoc/142028 (2019).
3. OECD Library. *The Future of Cooling,* Vol. 92 (International Energy Agency, 2018).
4. Woods, J. et al. Humidity's impact on greenhouse gas emissions from air conditioning. *Joule* **6**, 726–741 (2022).
5. Kitanovski, A. Energy applications of magnetocaloric materials. *Adv. Energy Mater.* **10**, 1903741 (2020).
6. Qian, X. et al. High-entropy polymer produces a giant electrocaloric effect at low fields. *Nature* **600**, 664–669 (2021).
7. Moya, X. & Mathur, N. D. Caloric materials for cooling and heating. *Science* **370**, 797–803 (2020).
8. Li, B. et al. Colossal barocaloric effects in plastic crystals. *Nature* **567**, 506–510 (2019).
9. Lloveras, P. et al. Colossal barocaloric effects near room temperature in plastic crystals of neopentylglycol. *Nat. Commun.* **10**, 1803 (2019).
10. Zhang, K. et al. Taming heat with tiny pressure. *Innov* **5**, 100577 (2024).
11. Wang, R. et al. Torsional refrigeration by twisted, coiled, and supercoiled fibers. *Science* **366**, 216–221 (2019).
12. Porta, M., Castán, T., Saxena, A. & Planes, A. Flexocaloric effect near a ferroelastic transition. *Phys. Rev. B* **104**, 94108 (2021).
13. Hou, H., Qian, S. & Takeuchi, I. Materials, physics, and systems for multicaloric cooling. *Nat. Rev. Mater.* **7**, 633–652 (2022).
14. Bonnot, E., Romero, R., Manosa, L., Vives, E. & Planes, A. Elastocaloric effect associated with the martensitic transition in shape-memory alloys. *Phys. Rev. Lett.* **100**, 125901 (2008).
15. Cui, J. et al. Demonstration of high efficiency elastocaloric cooling with large ΔT using NiTi wires. *Appl. Phys. Lett.* **101**, 073904 (2012).
16. Cong, D. et al. Colossal elastocaloric effect in ferroelastic Ni-Mn-Ti alloys. *Phys. Rev. Lett.* **122**, 255703 (2019).
17. Xie, Z., Sebald, G. & Guyomar, D. Comparison of direct and indirect measurement of the elastocaloric effect in natural rubber. *Appl. Phys. Lett.* **108**, 041901 (2016).
18. Ding, L. et al. Learning from superelasticity data to search for Ti-Ni alloys with large elastocaloric effect. *Acta Mater.* **218**, 117200 (2021).
19. Ossmer, H., Miyazaki, S. & Kohl, M. Elastocaloric heat pumping using a shape memory alloy foil device. In *2015 Transducers —2015 18th International Conference on Solid-State Sensors, Actuators and Microsystems, (TRANSDUCERS)* 726–729 (Anchorage, AK, 2015).
20. Brüederlin, F., Ossmer, H., Wendler, F., Miyazaki, S. & Kohl, M. SMA foil-based elastocaloric cooling—from material behavior to device engineering. *J. Phys. D. Appl. Phys.* **50**, 424003 (2017).
21. Ahčin, Ž. et al. High-performance cooling and heat pumping based on fatigue-resistant elastocaloric effect in compression. *Joule* **6**, 2338–2357 (2022).
22. Bachmann, N. et al. Long-term stable compressive elastocaloric cooling system with latent heat transfer. *Commun. Phys.* **4**, 194 (2021).
23. Ianniciello, L., Bartholomé, K., Fitger, A. & Engelbrecht, K. Long life elastocaloric regenerator operating under compression. *Appl. Therm. Eng.* **202**, 117838 (2022).
24. Snodgrass, R. & Erickson, D. A multistage elastocaloric refrigerator and heat pump with 28 K temperature span. *Sci. Rep.* **9**, 18532 (2019).
25. Zhang, J., Zhu, Y., Cheng, S., Yao, S. & Sun, Q. Enhancing cooling performance of NiTi elastocaloric tube refrigerant via internal grooving. *Appl. Therm. Eng.* **213**, 118657 (2022).
26. Li, X., Cheng, S. & Sun, Q. A compact NiTi elastocaloric air cooler with low force bending actuation. *Appl. Therm. Eng.* **215**, 118942 (2022).
27. Zhou, G., Zhu, Y., Yao, S. & Sun, Q. Giant temperature span and cooling power in elastocaloric regenerator. *Joule* **7**, 2003–2015 (2023).
28. Li, X., Hua, P. & Sun, Q. Continuous and efficient elastocaloric air cooling by coil-bending. *Nat. Commun.* **14**, 7982 (2023).
29. Qian, S. et al. Design, developement and testing of a compressive thermoelastic cooling system. In *The 24th IIR International Congress of Refrigeration*. 92 (IIR, 2015).
30. Qian, S. et al. Design of a hydraulically driven compressive elastocaloric cooling system. *Sci. Technol. Built Environ.* **22**, 500–506 (2016).
31. Brüederlin, F. et al. Elastocaloric cooling on the miniature scale: a review on materials and device engineering. *Energy Technol.* **6**, 1588–1604 (2018).
32. Qian, S. et al. High-performance multimode elastocaloric cooling system. *Science* **380**, 722–727 (2023).
33. Emaikwu, N. et al. Experimental investigation of a staggered-tube active elastocaloric regenerator. *Int. J. Refrig.* **153**, 370–377 (2023).

34. Chen, Y., Wang, Y., Sun, W., Qian, S. & Liu, J. A compact elastocaloric refrigerator. *Innov*. **3**, 100205 (2022).
35. Greibich, F. et al. Elastocaloric heat pump with specific cooling power of 20.9 W g–1 exploiting snap-through instability and strain-induced crystallization. *Nat. Energy* **6**, 260–267 (2021).
36. Sebald, G. et al. High-performance polymer-based regenerative elastocaloric cooler. *Appl. Therm. Eng.* **223**, 120016 (2023).
37. Zhang, S. et al. Solid-state cooling by elastocaloric polymer with uniform chain-lengths. *Nat. Commun.* **13**, 9 (2022).
38. Brüederlin, F., Bumke, L., Quandt, E. & Kohl, M. Cascaded SMA-Film Based Elastocaloric Cooling. In *2019 20th International Conference on Solid-State Sensors, Actuators and Microsystems & Eurosensors XXXIII (TRANSDUCERS & EUROSENSORS XXXIII)* 1467–1470 (Berlin, Germany, 2019).
39. Brüederlin, F. *Advanced Elastocaloric Cooling Devices Based on Shape Memory Alloy Films*. (Karlsruher Institut für Technologie (KIT), 2020).
40. Ulpiani, G. et al. Upscaling of SMA film-based elastocaloric cooling. *Appl. Therm. Eng.* **180**, 115867 (2020).
41. Schmidt, M., Schütze, A. & Seelecke, S. Scientific test setup for investigation of shape memory alloy based elastocaloric cooling processes. *Int. J. Refrig.* **54**, 88–97 (2015).
42. Kirsch, S.-M. et al. NiTi-based elastocaloric cooling on the macroscale: from basic concepts to realization. *Energy Technol.* **6**, 1567–1587 (2018).
43. Tušek, J. et al. A regenerative elastocaloric heat pump. *Nat. Energy* **1**, 16134 (2016).
44. Engelbrecht, K. et al. A regenerative elastocaloric device: experimental results. *J. Phys. D. Appl. Phys.* **50**, 424006 (2017).
45. Wang, Y. et al. Towards practical elastocaloric cooling. *Commun. Eng.* **2**, 79 (2023).
46. Cirillo, L., Greco, A. & Masselli, C. The energy performances of an elastocaloric device for air conditioning through numerical investigation. *Appl. Therm. Eng.* **236**, 121517 (2024).
47. Kabirifar, P. et al. Elastocaloric cooling: state-of-the-art and future challenges in designing regenerative elastocaloric. *Devices J. Mech. Eng.* **65**, 615–630 (2019).
48. Qian, S. et al. Not-in-kind cooling technologies: a quantitative comparison of refrigerants and system performance. *Int. J. Refrig.* **62**, 177–192 (2016).
49. Chen, J., Xing, L., Fang, G., Lei, L. & Liu, W. Improved elastocaloric cooling performance in gradient-structured NiTi alloy processed by localized laser surface annealing. *Acta Mater.* **208**, 116741 (2021).
50. Hou, H. et al. Fatigue-resistant high-performance elastocaloric materials made by additive manufacturing. *Science* **366**, 1116–1121 (2019).
51. Kim, Y., Jo, M.-G., Park, J.-W., Park, H.-K. & Han, H. N. Elastocaloric effect in polycrystalline Ni50Ti45.3V4.7 shape memory alloy. *Scr. Mater.* **144**, 48–51 (2018).
52. Chluba, C. et al. Ultralow-fatigue shape memory alloy films. *Science* **348**, 1004–1007 (2015).
53. Dang, P. et al. Low-fatigue and large room-temperature elastocaloric effect in a bulk $Ti_{49.2}Ni_{40.8}Cu_{10}$ alloy. *Acta Mater.* **229**, 117802 (2022).
54. Bumke, L., Zamponi, C., Jetter, J. & Quandt, E. Cu-rich $Ti_{52.8}Ni_{22.2}Cu_{22.5}Co_{2.5}$ shape memory alloy films with ultra-low fatigue for elastocaloric applications. *J. Appl. Phys.* **127**, 225105 (2020).
55. Fukuda, T., Saburi, T., Chihara, T. & Tsuzuki, Y. Mechanism of B2-B19-B19′ transformation in shape memory Ti–Ni–Cu Alloys. *Mater. Trans.* **36**, 1244–1248 (1995).
56. Dang, P. et al. Achieving stable actuation response and elastocaloric effect in a nanocrystalline $Ti_{50}Ni_{40}Cu_{10}$ alloy. *Scr. Mater.* **226**, 115263 (2023).
57. Dang, P. et al. Improved stability of superelasticity and elastocaloric effect in Ti-Ni alloys by suppressing Lüders-like deformation under tensile load. *J. Mater. Sci. Technol.* **146**, 154–167 (2023).
58. Qian, S. Thermodynamics of elastocaloric cooling and heat pump cycles. *Appl. Therm. Eng.* **219**, 119540 (2023).
59. Cook, B. A. et al. High-performance three-stage cascade thermoelectric devices with 20% efficiency. *J. Electron. Mater.* **44**, 1936–1942 (2015).
60. Dopazo, J. A. & Fernández-Seara, J. Experimental evaluation of a cascade refrigeration system prototype with CO_2 and NH_3 for freezing process applications. *Int. J. Refrig.* **34**, 257–267 (2011).

Acknowledgements

This work was financially supported by the National Natural Science Foundation of China (NSFC) under grant No. 52376015 (S.Q.), the National Natural Science Foundation of China (NSFC) under grant No. 52341601 (Y.H.), and the National Key Research and Development Program of China under grant No. 2021YFB3802104 (D.X.).

Author contributions

S.Q. and S.Y. conceived the concept. S.Y., Y.Li., Y.W., X.Z., and Y.Liu. developed and tested the elastocaloric refrigerator prototype. P.D. fabricated TiNiCu and evaluated materials properties. S.Y. and Y.Li. conducted simulations. S.Q., D.X., and Y.H. supervised the research. All authors contributed to the discussion of the results and writing.

Competing interests

The authors declare no competing interests.

Additional information

Supplementary information The online version contains supplementary material available at https://doi.org/10.1038/s41467-024-51632-y.

Correspondence and requests for materials should be addressed to Suxin Qian, Dezhen Xue or Ya-Ling He.

Peer review information *Nature Communications* thanks Jun Cui, Claudia Masselli, and the other, anonymous, reviewers for their contribution to the peer review of this work. A peer review file is available.